

# Zero Impact Parameter White Dwarf Collisions in FLASH

W.P. Hawley<sup>1</sup>, T. Athanassiadou<sup>1,2</sup>, F.X. Timmes<sup>1,2</sup>

Wendy.Hawley@asu.edu

Received \_\_\_\_\_; accepted \_\_\_\_\_

arXiv:1209.3749v1 [astro-ph.SR] 17 Sep 2012

---

<sup>1</sup>School of Earth and Space Exploration, Arizona State University, Tempe, AZ 85287, USA

<sup>2</sup>The Joint Institute for Nuclear Astrophysics, Notre Dame, IN 46556, USA

## ABSTRACT

We systematically explore zero impact parameter collisions of white dwarfs with the Eulerian adaptive grid code FLASH for  $0.64+0.64 M_{\odot}$  and  $0.81+0.81 M_{\odot}$  mass pairings. Our models span a range of effective linear spatial resolutions from  $5.2 \times 10^7$  to  $1.2 \times 10^7$  cm. However, even the highest resolution models do not quite achieve strict numerical convergence, due to the challenge of properly resolving small-scale burning and energy transport. The lack of strict numerical convergence from these idealized configurations suggest that quantitative predictions of the ejected elemental abundances that are generated by binary white dwarf collision and merger simulations should be viewed with caution. Nevertheless, the convergence trends do allow some patterns to be discerned. We find that the  $0.64+0.64 M_{\odot}$  head-on collision model produces  $0.32 M_{\odot}$  of  $^{56}\text{Ni}$  and  $0.38 M_{\odot}$  of  $^{28}\text{Si}$ , while the  $0.81+0.81 M_{\odot}$  head-on collision model produces  $0.39 M_{\odot}$  of  $^{56}\text{Ni}$  and  $0.55 M_{\odot}$  of  $^{28}\text{Si}$  at the highest spatial resolutions. Both mass pairings produce  $\sim 0.2 M_{\odot}$  of unburned  $^{12}\text{C}+^{16}\text{O}$ . We also find the  $0.64+0.64 M_{\odot}$  head-on collision begins carbon burning in the central region of the stalled shock between the two white dwarfs, while the more energetic  $0.81+0.81 M_{\odot}$  head-on collision raises the initial post-shock temperature enough to burn the entire stalled shock region to nuclear statistical equilibrium.

## 1. Introduction

Supernova Type Ia (SNIa) have continued to be foremost probes of the universe’s accelerating expansion (Riess et al. 1998; Perlmutter et al. 1999; Riess et al. 2011; Sullivan et al. 2011; Suzuki et al. 2012). While light curves between different SNIa vary, the

variations generally correlate with distance independent light-curve properties, such as the decline from B band maximum after 15 days (Phillips 1993). Calibration of the light curves onto a standard template yields distance indicators accurate to  $\sim 10\%$  (e.g., Silverman et al. 2012) and are primarily applied to SNIa not showing peculiarities (Branch et al. 1993). These “normal” SNIa presumably emerge from a homogeneous population of white dwarf progenitors. While the favored population is thought to be a carbon-oxygen white dwarf (WD) accreting matter from a non-degenerate companion star (e.g., Whelan & Iben 1973; Thielemann et al. 1986), recent observations suggest that a fraction of SNIa may derive from double-degenerate progenitors (Howell et al. 2006; Hicken et al. 2007; Gilfanov & Bogdán 2010; Bianco et al. 2011).

In view of these and other observations of SNIa progenitor systems, recent theoretical studies have explored double degenerate mergers and collisions of white dwarfs as potential progenitors of SNIa (Guerrero et al. 2004; Yoon et al. 2007; Maoz 2008; Lorén-Aguilar et al. 2009; Raskin et al. 2009; Rosswog et al. 2009; Lorén-Aguilar et al. 2010; Pakmor et al. 2010; Raskin et al. 2010; Shen et al. 2012; Pakmor et al. 2012). Almost all of these efforts use smooth particle hydrodynamic (SPH) codes to model most of the collision or merger process. SPH and Eulerian grid codes, such as FLASH (Fryxell et al. 2000), have well-known complimentary strengths and weaknesses – particle codes are inherently better at angular momentum conservation, whereas grid codes have a superior treatment of shocks. Only Rosswog et al. (2009) included a zero impact parameter white dwarf collision model with FLASH. They used a mirror gravitational potential for one white dwarf at one spatial resolution. They found their FLASH calculations yielded about half as much  $^{56}\text{Ni}$  as the equivalent SPH calculation ( $0.32 M_{\odot}$  for SPH,  $0.16 M_{\odot}$  for FLASH).

In this paper, we use the Eulerian adaptive mesh refinement code FLASH to model the zero impact collisions between  $0.64+0.64 M_{\odot}$  and  $0.81+0.81 M_{\odot}$  carbon-oxygen white dwarf

mass pairings. Like the single case studied by Rosswog et al. (2009), our configurations are highly idealized cases of head-on collisions between identical, initially spherical white dwarfs. One aim of our paper is to determine whether or not, given presently available computing resources and numerical algorithms, simulations of collisions can be used to reliably predict the fraction of white dwarf material that is converted by explosive nucleosynthesis into heavier elements such as silicon and nickel. Other efforts have focused on the realism of the initial conditions and subsequent evolution, including but limited to, in-spiraling from a binary orbit (Rasio & Shapiro 1995; Pakmor et al. 2010; Dan et al. 2011; Raskin et al. 2012), unequal mass collisions (Benz et al. 1989, 1990; Rosswog et al. 2009; Lorén-Aguilar et al. 2010; Raskin et al. 2010; Pakmor et al. 2012), and the final long-term fate of merged systems (van Kerkwijk et al. 2010; Yoon et al. 2007; Shen et al. 2012). Our simulations, through their idealized nature, highlight the essential physics and numerical convergence properties of the simplest possible configuration. In addition, our idealized configurations form a baseline for further studies that incorporate more realistic initial conditions.

Our paper is organized as follows. In §2, we describe the input physics, initial conditions, and boundary conditions of our FLASH simulations. In §3, we discuss the results of our studies over a range of spatial resolutions and time-step choices, and in §4 we explore the implications of our results and describe directions for future studies.

## 2. Input Physics, Initial Conditions, and Boundary Conditions

Our 3D simulations are carried out with FLASH 3.2, a 3D Eulerian hydrodynamics code with adaptive mesh refinement (Fryxell et al. 2000; Calder et al. 2002). We use the included Helmholtz equation of state (Timmes & Swesty 2000), the 13 isotope alpha-chain reaction network that includes isotopes from  $^4\text{He}$  to  $^{56}\text{Ni}$  to model energy generation from nuclear burning (Timmes 1999), and the multigrid Poisson gravity solver with Dirichlet

boundaries (Ricker 2008). All the simulation domain boundaries use a diode boundary condition, which is a zero-gradient boundary condition where fluid velocities are not allowed to point back into the domain. We follow both white dwarfs in 3D rectilinear coordinates throughout calculation, rather than using a mirror gravitational potential and evolving one white dwarf (as used in Rosswog et al. 2009).

Our initial 1D white dwarf profiles are calculated assuming hydrostatic equilibrium and mass conservation<sup>1</sup>. Our initial white dwarf models use the same equation of state as in FLASH, namely, the Helmholtz equation of state. We assume a uniform composition of 50%  $^{12}\text{C}$  and 50%  $^{16}\text{O}$ . We use white dwarfs with masses  $0.64$  and  $0.81 M_{\odot}$ , to match the masses used in Raskin et al. (2010), with an isothermal temperature of  $10^7$  K. We map the 1D white dwarf profiles for the density, temperature and composition onto a 3D rectilinear Cartesian grid. Our computational domain is a cubic box chosen to be eight times the white dwarf radius (see Fig. 1). The white dwarfs are initially placed four white dwarf radii apart from center to center, which is large enough to allow the subsequent evolution to produce tidal distortions while allowing sufficient numerical resolution in the central regions.

The symmetry of head-on collisions between identical, initially spherical white dwarfs suggests 2D axisymmetric simulations may have been sufficient. Our rationale for deploying 3D rectilinear coordinates is three-fold. First, we want to explicitly show that FLASH maintains symmetry throughout the collision and subsequent explosion processes. Second, we want to compare our results on this important numerical test case with other existing 3D calculations (both grid and particle). Imposing axisymmetric conditions would have complicated these comparisons because we would not know if differences from existing 3D models were driven by different physics, different numerics or the imposition of axisymmetry itself. Third, we anticipate exploring unequal mass and non-zero impact parameter collision

---

<sup>1</sup>Code available from [http://cococubed.asu.edu/code\\_pages/coldwd.shtml](http://cococubed.asu.edu/code_pages/coldwd.shtml)

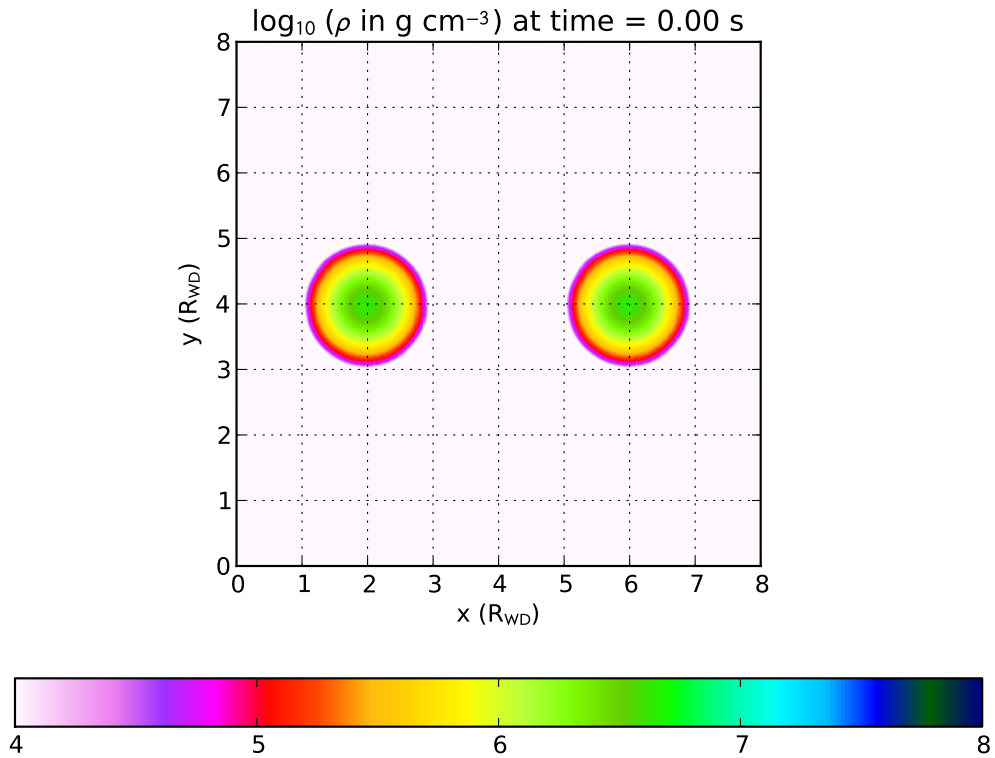


Fig. 1.— A 2D slice of density through the x-y mid-plane at  $t=0.0$  s for the  $0.64+0.64 M_{\odot}$  collision. Each tick mark has a value of one white dwarf radius, which is  $8.3 \times 10^8$  cm. The size of the domain is equal to eight white dwarf radii, and the white dwarfs are positioned four white dwarf radii apart from center to center.

models with FLASH, both of which violate axisymmetry. To better assess the impact of these effects requires an equal mass, zero impact parameter, 3D benchmark calculation.

We use the free-fall expression for the initial, relative speed of the two white dwarfs,  $v = [2G(M_1 + M_2)/\Delta r]^{1/2}$ , where  $M_i$  are the masses of the constituent white dwarfs and  $\Delta r$  is the initial separation of their centers of mass, which for our initial conditions is  $4R_{\text{WD}}$ . Each white dwarf moves toward the other white dwarf, one in the positive x-direction and the other in the negative x-direction, with half of the relative speed. The centers of both stars lie on the x-axis, and thus the initial velocities are purely in the x-direction.

The surrounding ambient medium is set to the same temperature as the isothermal white dwarfs with a density that is small ( $10^{-4}$  g cm $^{-3}$ ) compared to the density of the outermost regions of the white dwarf ( $\sim 1$ - $10$  g cm $^{-3}$ ). Table 1 lists the initial conditions for each of our six simulations.

Table 1: Initial Conditions for the 3D FLASH models. Columns are the run number, white dwarf masses ( $M_1, M_2$ ), maximum level of refinement ( $l$ ), maximum spatial resolution ( $R$ ), domain size ( $D$ ), white dwarf initial velocities ( $v_1, v_2$ ), the value of the timestep limiter ( $f$ ), white dwarf radii ( $R_{\text{WD}}$ ), and central white dwarf densities ( $\rho_{\text{WD}}$ ).

#	$M_1, M_2$ ( $M_\odot$ )	$l$	$R$ ( $10^7$ cm)	$D$ ( $10^9$ cm)	$v_1, v_2$ ( $10^8$ cm s $^{-1}$ )	$f$	$R_{\text{WD}}$ ( $10^8$ cm)	$\rho_{\text{WD}}$ ( $10^6$ g cm $^{-3}$ )
1	0.64	5	5.19	6.64	$\pm 1.59$	0.2	8.30	4.51
2	0.64	6	2.59	6.64	$\pm 1.59$	0.2	8.30	4.51
3	0.64	7	1.30	6.64	$\pm 1.59$	0.2	8.30	4.51
4	0.81	5	4.32	5.51	$\pm 1.97$	0.2	6.88	11.2
5	0.81	6	2.16	5.51	$\pm 1.97$	0.3	6.88	11.2
6	0.81	7	1.08	5.51	$\pm 1.97$	0.3	6.88	11.2

Our FLASH models begin with 1 top-level initial block, where each block contains 8 cells in each direction  $(x, y, z)$ . The blocks are refined or derefined at each time-step based on changes in density and pressure. For each successive level of refinement, the block size decreases by a factor of two, creating a nested block structure. At maximum refinement, the smallest block size is determined by  $R = D/(8 \times 2^{l-1})$ , where  $D$  is the domain size in one dimension and  $l$  is the maximum level of refinement as seen in Table 1. At first contact between the white dwarfs, shock waves are sent into the ambient medium, causing the grid in the ambient medium to rapidly become maximally refined. To avoid concentrating resources on these less interesting regions of the models, we use a derefine procedure at first contact that sets a radius equal to 1.2 white dwarf radii beyond which the blocks in the ambient material are forced to be less refined than the blocks in the collision region.

The nuclear reaction network in FLASH uses constant thermodynamic conditions over the course of a timestep. However, the Courant limited hydrodynamic timestep may be so large compared to the burning timescale that the nuclear energy released in a cell may exceed the existing specific internal energy. To ensure the hydrodynamics and burning remain coupled, as well as to capture the strong temperature dependence of the nuclear reaction rates, we limit the timestep as a result of nuclear burning by a factor  $f$ , which constrains the maximum allowable change in specific internal energy. The overall timestep is  $dt_{n+1} = \min[dt_{\text{hydro}}, dt_{\text{burn}}]$ , where

$$dt_{\text{burn}} = dt_n \times f \times \frac{u_{n-1}^i}{u_n^i - u_{n-1}^i}, \quad (1)$$

where the subscript  $n$  refers to the timestep number,  $dt_{\text{hydro}}$  is the hydrodynamic timestep,  $dt_{\text{burn}}$  is the burning timestep, and  $u^i$  is the specific internal energy of the  $i$ th cell. Table 1 lists the nominal values of  $f$  used for our six simulations, and the effects of using different values of  $f$  is discussed in §3.2.



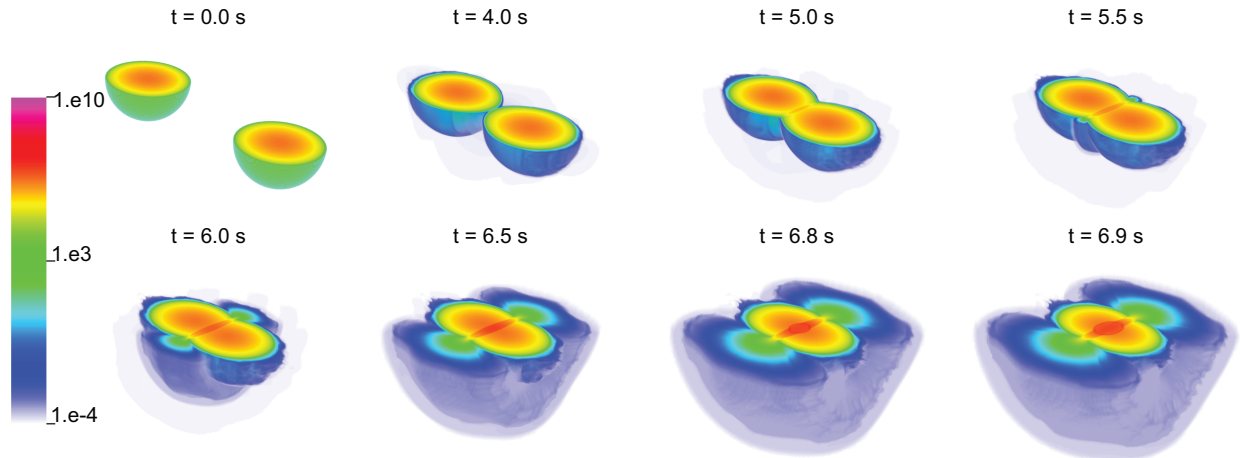


Fig. 2.— 3D images cut through the center of the  $y$ -axis of the  $2 \times 0.64$  collision density from first contact at 0.0 s to after ignition at 6.9 s. For scale, each white dwarf has a radius of  $8.3 \times 10^8$  cm. The density colorbar is logarithmic and extends from  $10^{-4}$  to  $10^{10}$   $\text{g cm}^{-3}$ .

### 3. Results

#### 3.1. General Features of the Collision Models

Zero impact parameter, or head-on, white dwarf collisions undergo four distinct phases of evolution. First, the white dwarfs become tidally distorted as they approach each other. For the  $0.64 + 0.64 M_{\odot}$  case (hereafter  $2 \times 0.64$ ), the velocity gradient across the white dwarf at first contact ranges from about  $3500 \text{ km s}^{-1}$  to  $5000 \text{ km s}^{-1}$ . Second, a shock wave is produced normal to the  $x$ -axis at first contact. The shock stalls because the speed of infalling material and the sound speed are comparable. Third, nuclear burning is initiated within the stalled shock region. Finally, the nuclear energy released unbinds the system, leading eventually to homologous expansion.

An overview of the evolution of the  $2 \times 0.64$  collision is shown in Fig. 2. The 3D

calculation has been sliced through the x-z mid-plane to show detail at the center of the collision. Due to the symmetry of a head-on collision, a cut through the x-z mid-plane will look identical to a cut through the x-y mid-plane. The top panel of the figure represents four times in the collision from the start of the simulation ( $t=0.0$  s), to first contact ( $t=4.0$  s), to the formation of the stalled shock region ( $t=5.0$  s), and finally, to the jettisoning of material orthogonal to the x-axis ( $t=5.5$  s).

Given the white dwarf radius and initial velocity shown in Table 1 for the  $2 \times 0.64$  collision, the time to first contact would be  $2R/v=5.2$  s if the initial speed was constant and the white dwarfs remained spherical. However, the initial speed increases due to gravitational acceleration and tidal distortion causes the white dwarfs to become elongated along the x-axis. As a result the two white dwarfs experience first contact sooner, at about 4.0 s.

The bottom panel represents the the further progression of the collision from the continued jettison of material ( $t=6.0$  s), to just before ignition (6.5 s), to just after ignition ( $t=6.8$  s), and finally to the spread of nuclear burning through the white dwarfs ( $t=6.9$  s). These steps are discussed in further detail below.

Fig. 3 shows the thermodynamic, mechanical, and morphological properties of the  $2 \times 0.64$  head-on collision model. At 6.00 s after the beginning of the model, the white dwarfs are past first contact but have not yet begun runaway nuclear burning. The right panel shows the mass density profiles of a slice through the simulation in the x-y plane. In addition to the ambient medium (white in the figure), there are two distinct regions of density: the uncollided white dwarf material and the stalled shock region. The density and temperature are not yet high enough to fuel runaway burning. The lower left panel of Fig. 3 shows these quantities as well as the sound speed and velocity in the x-direction along a line connecting the centers of the two white dwarfs and parallel to the x-axis. The

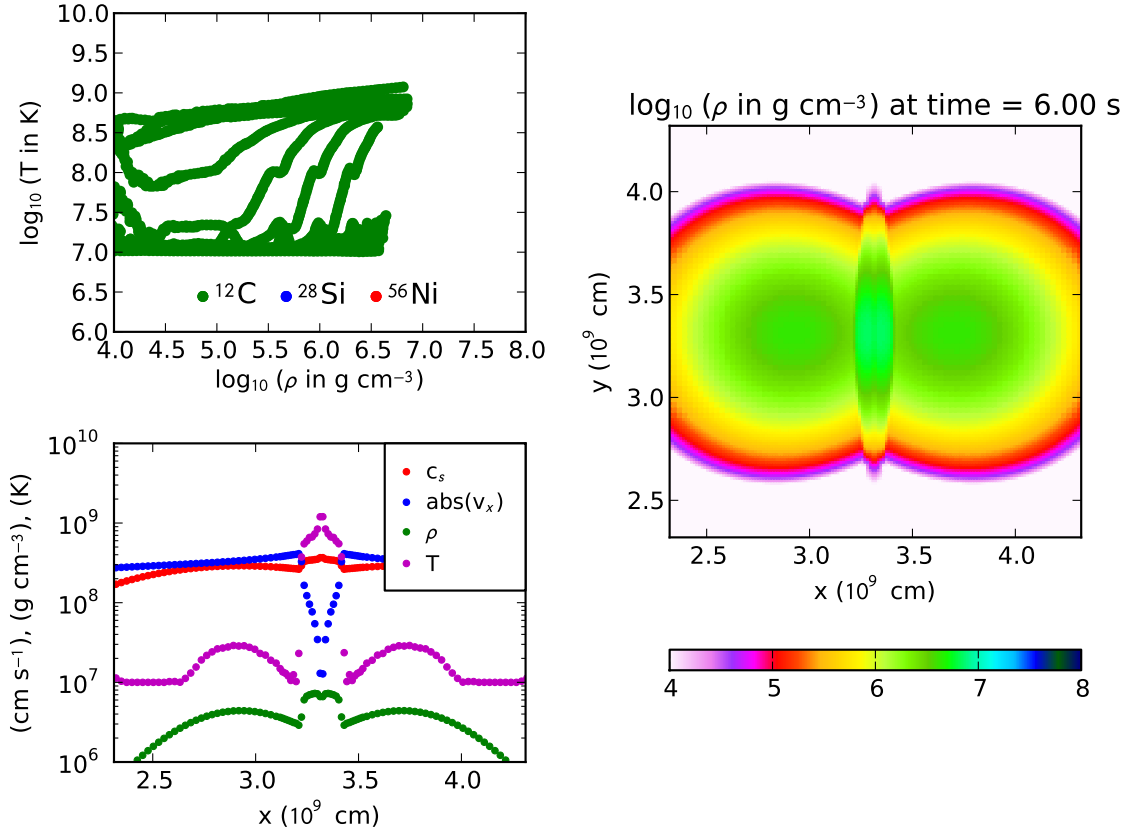


Fig. 3.— Analysis images of the  $2 \times 0.64$  collision at  $t=6.00 \text{ s}$ , after first contact, but before ignition. Top-left: Locations of all cells in the density-temperature plane. The color of the points represents the primary composition of the corresponding cell: green for  $^{12}\text{C}$ , blue for  $^{28}\text{Si}$ , and red for  $^{56}\text{Ni}$ . The data are binned into 100 equally spaced bins in logarithmic density and temperature. Bottom-left: Temperature, x-velocity, density, and sound speed along the x-axis. Right: A 2D slice of density through the x-y mid-plane.

sound speed is lower than the infall velocity speed, causing the stalling of the shock region. The temperature profile peaks at  $\approx 10^9$  K, which is not hot enough to reach the carbon burning threshold. The upper left panel of Fig. 3 shows the state of the collision in the density-temperature plane. The color of the points represents the primary composition of the corresponding cell; green for  $^{12}\text{C}$ , blue for  $^{28}\text{Si}$ , and red for  $^{56}\text{Ni}$ . Material with  $T \approx 10^7$  K represents the cold and dense parts of the two stars that have not yet collided. The region with  $10^7 < T < 10^9$  K and  $10^4 < \rho < 10^{6.5}$  g cm $^{-3}$ , represents the shocked material. At this point in the collision, “tracks” run from the lower left to the upper right, representing tori of material orthogonal to the x-axis at the center of the collision. In this case,  $^{28}\text{Si}$  and  $^{56}\text{Ni}$  have not yet been produced, thus all the cells are primarily composed of  $^{12}\text{C}$ .

Fig. 4 has the same format as Fig. 3 at 6.60 s when runaway nuclear burning has begun. On the right panel, there are three distinct regions of the collision at this point in time: the white dwarf material which has not yet experienced the collision; the lenticular, nearly isobaric, stalled shock region; and the central region where a detonation has begun to propagate. The detonation front is outlined by the darker colored (higher density) oval region in Figs. 4. Our FLASH simulations do not resolve the initiation of the detonation. Instead, at all spatial resolutions investigated, the central-most cell in the  $2 \times 0.64$  head-on collision model undergoes runaway carbon burning which begins to propagate a detonation.

In the lower left panel of Fig. 4, again, three distinct regions are visible - the unshocked white dwarfs the stalled shock, and the central-most detonation region. The temperature in the unshocked white dwarf material rises smoothly from the initially imposed background temperature of  $1 \times 10^7$  K to  $\approx 3 \times 10^7$  K at the centers of both white dwarfs because of low-amplitude velocity waves sloshing around the white dwarf interiors. However,  $3 \times 10^7$  K is well below the carbon burning threshold, does not lift the electron degeneracy of the material, and does not impact our results. In the unshocked region, the infall speed

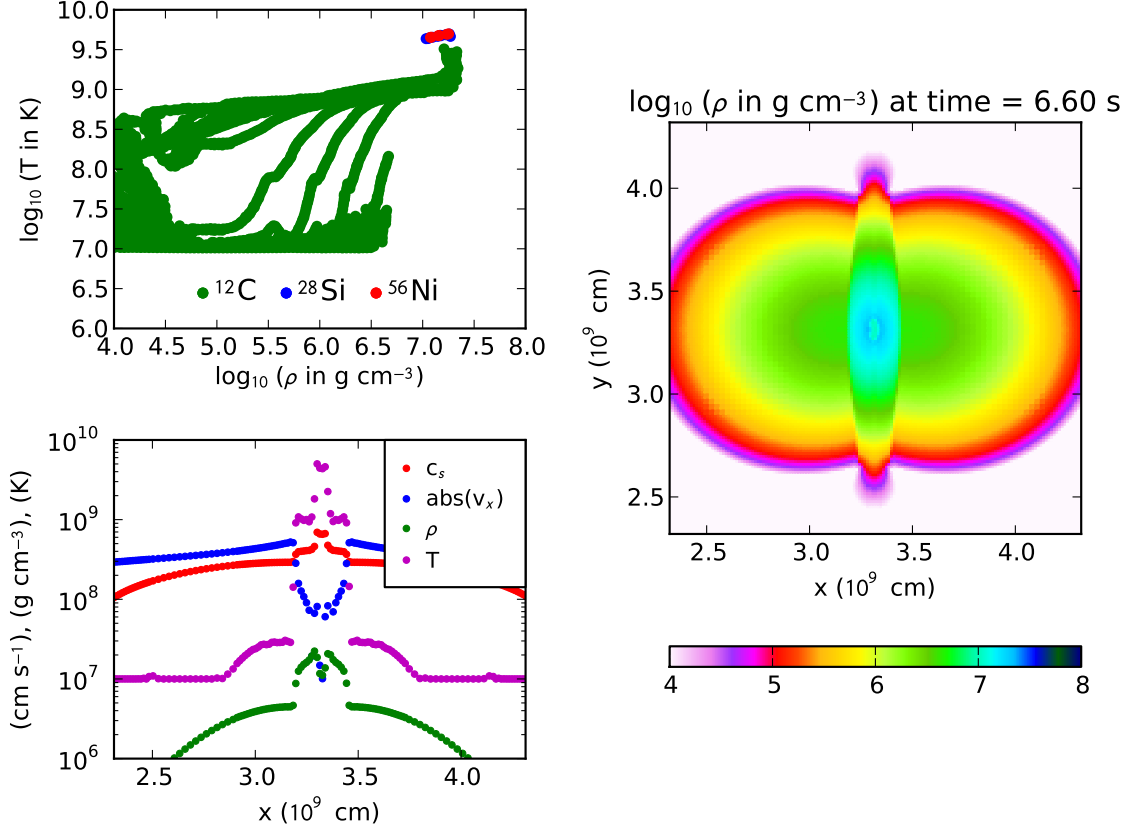


Fig. 4.— Same format as Fig. 3, when the model is at  $t=6.60 \text{ s}$ , right after ignition.

of material is greater than the local sound speed. The material behind the stalled shock reaches temperatures that are sufficient to lift electron degeneracy and are just below the carbon burning threshold of  $\approx 2 \times 10^9 \text{ K}$ . The density in the stalled shock region reaches a peak of  $\approx 2 \times 10^7 \text{ g cm}^{-3}$ . In the innermost region where a detonation front has traveled  $\sim 5 \times 10^7 \text{ cm}$  from the center, the temperature is  $\approx 6 \times 10^9 \text{ K}$  and the density dips to  $\approx 1 \times 10^7 \text{ g cm}^{-3}$ . In the upper left panel of Fig. 4, hot, dense material with  $T > 10^9 \text{ K}$  and  $\rho > 10^7 \text{ g cm}^{-3}$  from the central regions of the collision are in the upper right corner where the original carbon material has burned to  $^{28}\text{Si}$  and  $^{56}\text{Ni}$ .

Fig. 5 has the same format as Fig. 3 and the right panel shows the density profile when the detonation front has traveled outward from the center and the densest parts of the white dwarfs are about to enter the stalled shock region. The upper left panel indicates that more  $^{12}\text{C}$  material is present in the high density regime with  $\rho > 10^7 \text{ g cm}^{-3}$ , and being burned to  $^{28}\text{Si}$  and  $^{56}\text{Ni}$ . The lower left panel shows that the sound speed in the burned region is comparable with the speed of the infalling material, and the width of the detonation has expanded.

As additional energy from nuclear burning is added, the double white dwarf system eventually becomes gravitationally unbound. Fig. 6 has the same format as Fig. 4. The right panel shows the density distribution of the system slightly before the explosion reaches homologous expansion. The innermost  $10^9 \text{ cm}$  reaches a nearly constant temperature of  $\approx 3 \times 10^9 \text{ K}$  with a slowly varying density distribution that peaks at  $\approx 5 \times 10^6 \text{ g cm}^{-3}$ . The density-temperature plot in the upper left panel indicates larger amounts of high density, high temperature material with  $\rho > 10^6 \text{ g cm}^{-3}$  and  $T > 10^9 \text{ K}$ . More material has achieved the conditions necessary to synthesize  $^{28}\text{Si}$  (blue) and  $^{56}\text{Ni}$  (red). The lower left panel shows the sound speed is always greater than the infall speed of the remaining material.

The  $0.81\text{-}0.81 M_{\odot}$  (hereafter  $2 \times 0.81$ ) collision models evolve through a similar set of stages as the  $2 \times 0.64$  collision models, except the larger kinetic energy at impact is sufficient for the initial shock to raise the temperature well above the  $^{12}\text{C}+^{12}\text{C}$  threshold. Fig. 7 shows that the entire stalled shocked region burns rapidly to a state of nuclear statistical equilibrium and achieves a nearly isothermal state. Central ignition does not occur because the  $^{12}\text{C}+^{16}\text{O}$  material has already been burned to nuclear statistical equilibrium. We discuss this difference in additional detail in §3.3.

Otherwise, the stages of the  $2 \times 0.81$  collision are very similar to the evolution of the  $2 \times 0.64$  collision seen above, with the  $2 \times 0.81$  collision producing a greater amount of  $^{56}\text{Ni}$ .

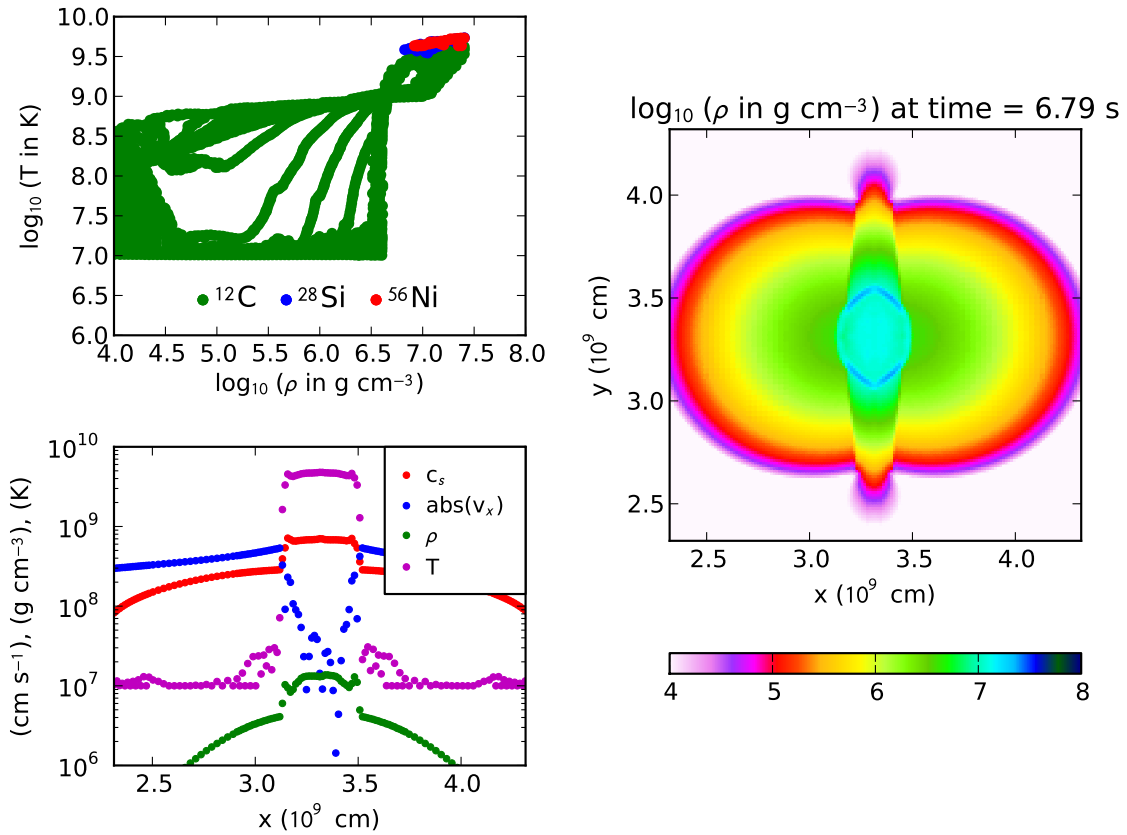


Fig. 5.— Same format as Fig. 3, when the model is at  $t=6.79 \text{ s}$ , as the stalled shock region slightly expands and the densest parts of the white dwarfs begin to enter the stalled shock region.

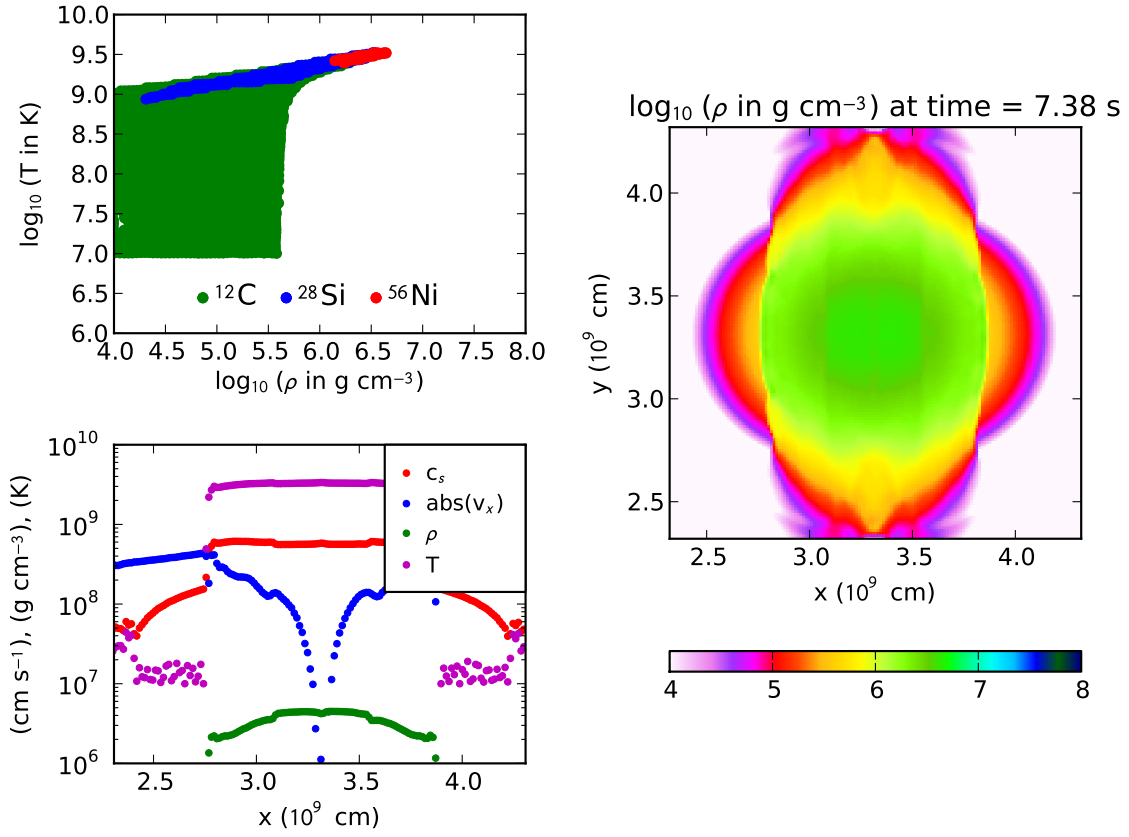


Fig. 6.— Same format as Fig. 3 at  $t=7.38 \text{ s}$ , just before the system becomes gravitationally unbound.



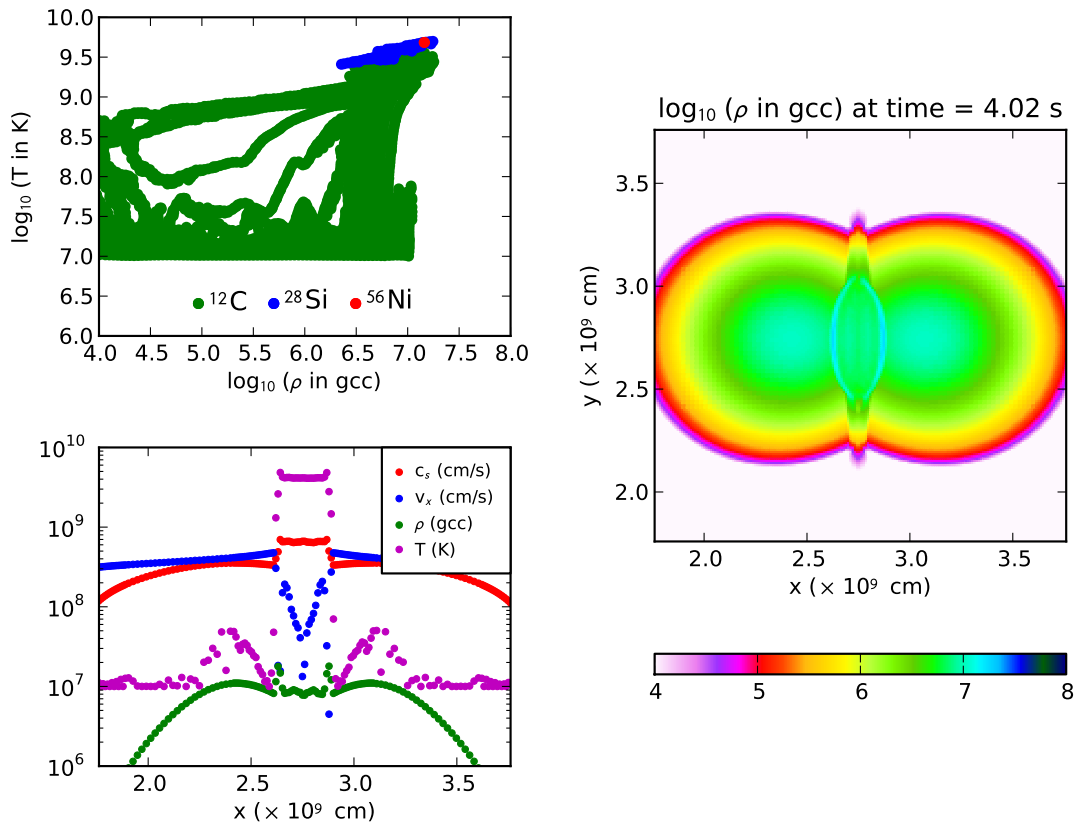


Fig. 7.— Same format as Fig. 3 at  $t=4.02 \text{ s}$  for the  $2 \times 0.81$  collision model.

### 3.2. Numerical Convergence

To assess the numerical convergence, we performed the  $2\times 0.64$  and  $2\times 0.81$  simulations at three different spatial resolutions. Each increase in spatial resolution is a factor of two more refined in one dimension, a factor of eight in volume (see Table 1), and takes at least twice as many time steps depending on the burning timestep. As the spatial resolution increases, the cells that are burning carbon to heavier elements become smaller in volume and the timestep decreases, leading to improved coupling between the hydrodynamics and nuclear burning.

Table 2 lists the ejected masses for each of the six convergence simulations and Fig. 8 shows the convergence behavior of  $^{12}\text{C}+^{16}\text{O}$ ,  $^{28}\text{Si}$ ,  $^{56}\text{Ni}$  yields, as well as the internal energy, kinetic energy, and the total energy at the end of the simulation. The upper plot in Fig. 8 shows that for the  $2\times 0.64$  collision the  $^{56}\text{Ni}$  mass (dashed red) increases, the  $^{28}\text{Si}$  mass (dashed blue) decreases, and the  $^{12}\text{C}+^{16}\text{O}$  (dashed green) decreases as the spatial resolution increases. The percent change in  $^{56}\text{Ni}$  production is 138% between the  $R = 5.19 \times 10^7$  cm and  $R = 2.59 \times 10^7$  cm models, and 3.3% between the the  $R = 2.59 \times 10^7$  cm and  $R = 1.30 \times 10^7$  cm models. Although higher resolution models are needed to reach numerical convergence, the  $^{56}\text{Ni}$  mass is approaching convergence at  $0.32 M_{\odot}$  (see Table 2). The internal energy (solid green) at the end of the  $2\times 0.64$  collision simulation decreases with increasing spatial resolution, but the kinetic energy (solid blue) when the model terminates increases with increasing spatial resolution. The net result is that the total energy (solid red) is nearly constant over the range of resolutions explored.

The lower panel in Fig. 8 shows that for the  $2\times 0.81$  collision the  $^{56}\text{Ni}$  mass decreases, the  $^{28}\text{Si}$  mass increases as the spatial resolution increases, and the  $^{12}\text{C}+^{16}\text{O}$  slightly decreases. Although convergence has not been achieved, the  $^{56}\text{Ni}$  mass is approaching convergence at  $0.39 M_{\odot}$  (see Table 2). We discuss the reason for the different convergence

Table 2: Ejected Masses.

$M_1, M_2$	$R$	$^{12}\text{C} + ^{16}\text{O}$	$^{28}\text{Si}$	$^{56}\text{Ni}$
( $M_\odot$ )	( $10^7$ cm)	( $M_\odot$ )	( $M_\odot$ )	( $M_\odot$ )
0.64	5.19	0.29	0.45	0.13
0.64	2.59	0.21	0.37	0.31
0.64	1.30	0.19	0.37	0.32
0.81	4.32	0.19	0.41	0.62
0.81	2.16	0.19	0.50	0.45
0.81	1.08	0.18	0.53	0.39

trends between the  $2 \times 0.64$  and  $2 \times 0.81$  cases below. The internal energy and kinetic energy at the end of the  $2 \times 0.81$  collision simulations appears to be oscillating towards convergence as the spatial resolution is increased. As a consequence of the internal energy and kinetic energy being out of phase, the total energy is nearly constant over the range of resolutions explored.

Although strict numerical convergence has not been achieved with these six simulations, some trends can be seen. As the total mass of the binary system increases in zero impact parameter collisions, the  $^{56}\text{Ni}$  mass increases, indicating that larger mass collisions will produce more  $^{56}\text{Ni}$ . For both mass pairs at highest resolution,  $\approx 0.2 M_\odot$  of unburned  $^{12}\text{C} + ^{16}\text{O}$  was ejected.

Higher numerical resolutions are desirable, but prohibitively expensive for this study, as our most resolved 3D models required at least 200,000 CPU hours per run. Simulations with higher spatial resolution are not possible in the context of the current study because doubling the grid resolution in a 3D simulation effectively increases the number of cells by a factor of  $\approx 2^3$  and the number of timesteps by a factor of 2, meaning

over an order-of-magnitude increase in computational time. Although these effects can be ameliorated somewhat by adopting more aggressive derefinement criteria, further restricting the computational domain size, or relaxing the timestep controller  $f$ , we expect that increasing the maximum resolution another factor of two ( $6.5 \times 10^6$  cm for the  $2 \times 0.64$  models and  $5.04 \times 10^6$  cm for the  $2 \times 0.81$  models) would require  $\approx 2$  million CPU hours per run, which is beyond our capabilities here.

Reducing the timestep limiting factor,  $f$ , and thereby reducing the timestep during nuclear burning changes the amount of  $^{56}\text{Ni}$  produced. For example, changing from  $f=0.5$  to  $f=0.1$  in the  $2 \times 0.64$  simulation with a spatial resolution of  $R = 2.59 \times 10^7$  cm causes the  $^{56}\text{Ni}$  production to increase by approximately  $0.1 M_{\odot}$ , a 30% change. Fig. 9 shows the evolution of the hydrodynamic time step (solid lines), burning time step (dotted lines), and  $^{56}\text{Ni}$  mass (dashed lines) for the 5-level (red), 6-level (green), and 7-level (blue)  $2 \times 0.81$  collisions. We use  $f=0.2$  for the 5-level run and  $f=0.3$  for the 6- and 7-level runs to force the burning timestep to fall below the hydrodynamic timestep during the  $^{56}\text{Ni}$  production phase. In all our simulations, we set  $f$  such that  $dt_{\text{burn}} \approx 0.01 dt_{\text{hydro}}$  during the phase of evolution when nuclear burning is significant. Setting  $f$  to smaller values greatly increases the computing time without having a significant effect on the nucleosynthesis yields.

Fig. 8 shows that the  $2 \times 0.64$  collision produces more  $^{56}\text{Ni}$  as spatial resolution increases. To understand this behavior we examine profiles along the x-axis of the density and temperature for 5-, 6-, and 7-levels of refinement. The upper panel of Fig. 10 shows the three models with different spatial resolutions for the  $2 \times 0.64$  collision at 5.6 s. The shocked region is widest in the 5-level model, and narrower in the 6- and 7-level models. The density is smaller (just below  $3 \times 10^6$  g cm $^{-3}$ ) and nearly constant for the 5-level model, larger for the 6-level model than the 5-level model ( $3.5 \times 10^6$  g cm $^{-3}$ ), and slightly larger for the 7-level model than the 6-level model ( $3.6 \times 10^6$  g cm $^{-3}$ ). Both the 6- and 7-level models

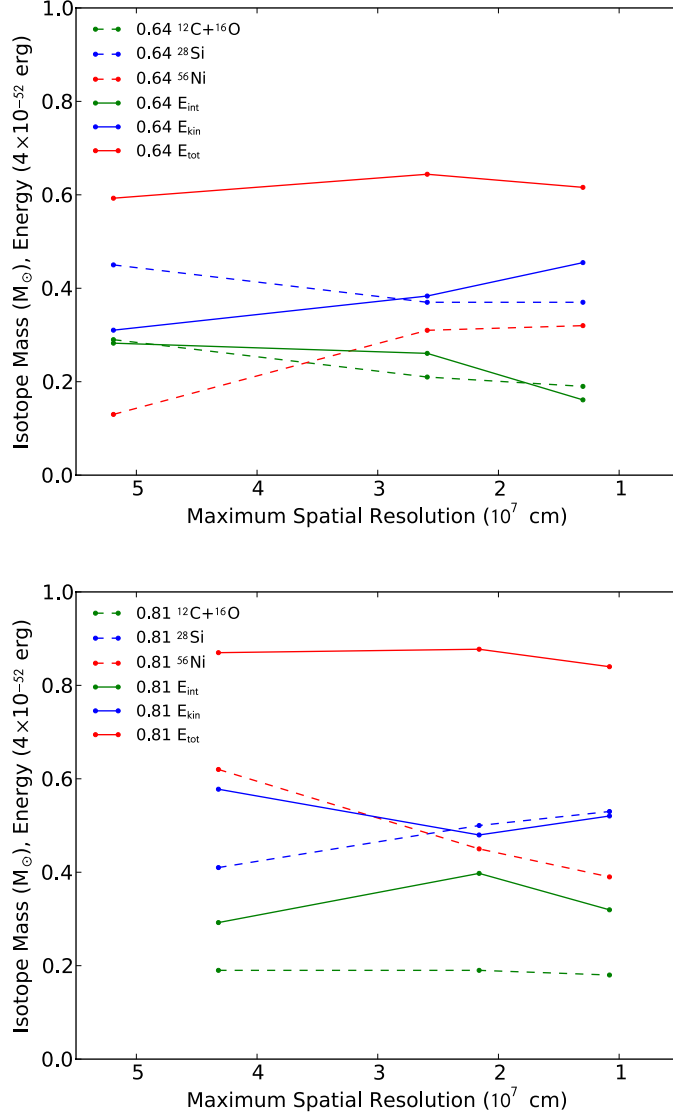


Fig. 8.— Convergence plot for the  $2 \times 0.64$  (top) and  $2 \times 0.81$  (bottom) head-on collisions. Points from left to right correspond to 5-, 6-, and 7-level runs for each collision. The dashed line colors represent different isotopes, where blue corresponds to  $^{28}\text{Si}$ , green to  $^{12}\text{C}+^{16}\text{O}$ , and red to  $^{56}\text{Ni}$ . The solid line colors represent internal energy (green), kinetic energy (blue), and total energy (red).

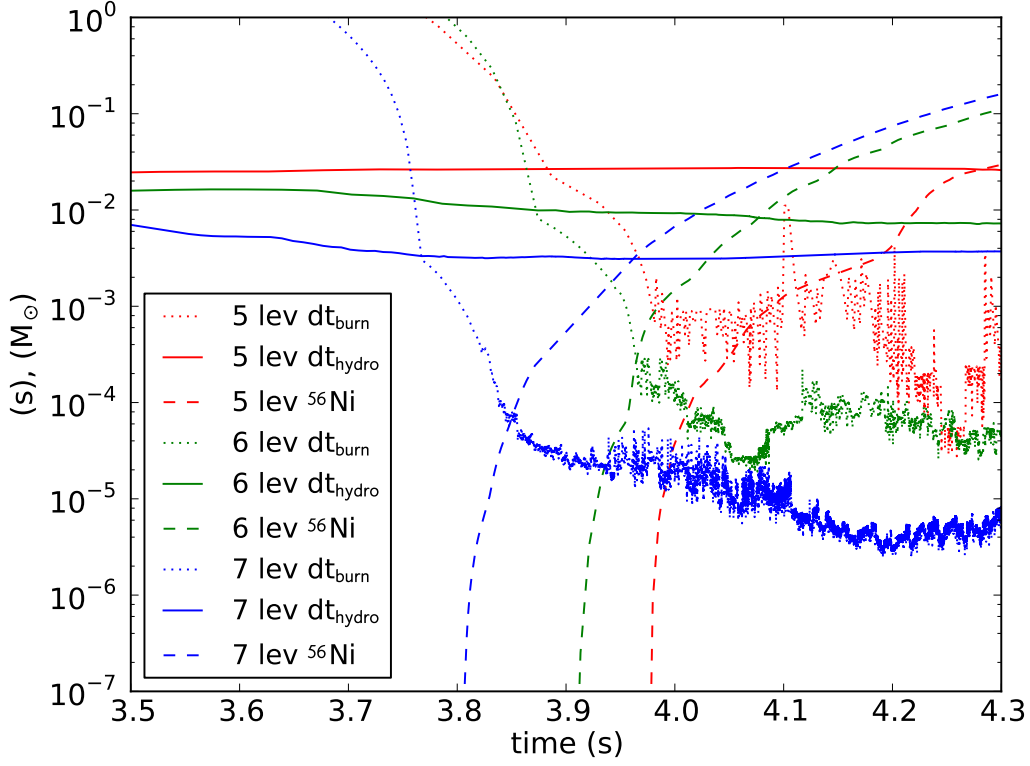


Fig. 9.— Evolution of the hydrodynamic time step (solid line), burning time step (dotted line), and  $^{56}\text{Ni}$  mass (dashed line) for the 5-level (red), 6-level (green), and 7-level (blue) models of the  $2 \times 0.81$  collision.

show a small valley in the central density. The peak temperature is smaller for the 5-level ( $\approx 10^9$  K), and slightly higher for the 6-level and 7-level models (both above  $10^9$  K).

At 6.4 s (middle panel in Fig. 10), the density and temperature profile patterns as described for 5.6 s generally still hold, but the peak temperature is now the same for all three levels of refinement ( $\approx 1.5 \times 10^9$  K). Detonation occurs just after this time frame (as seen below). Thus, we expect to see more  $^{56}\text{Ni}$  produced for the 6-level and 7-level models than for the 5-level model because there is more material in the shocked region

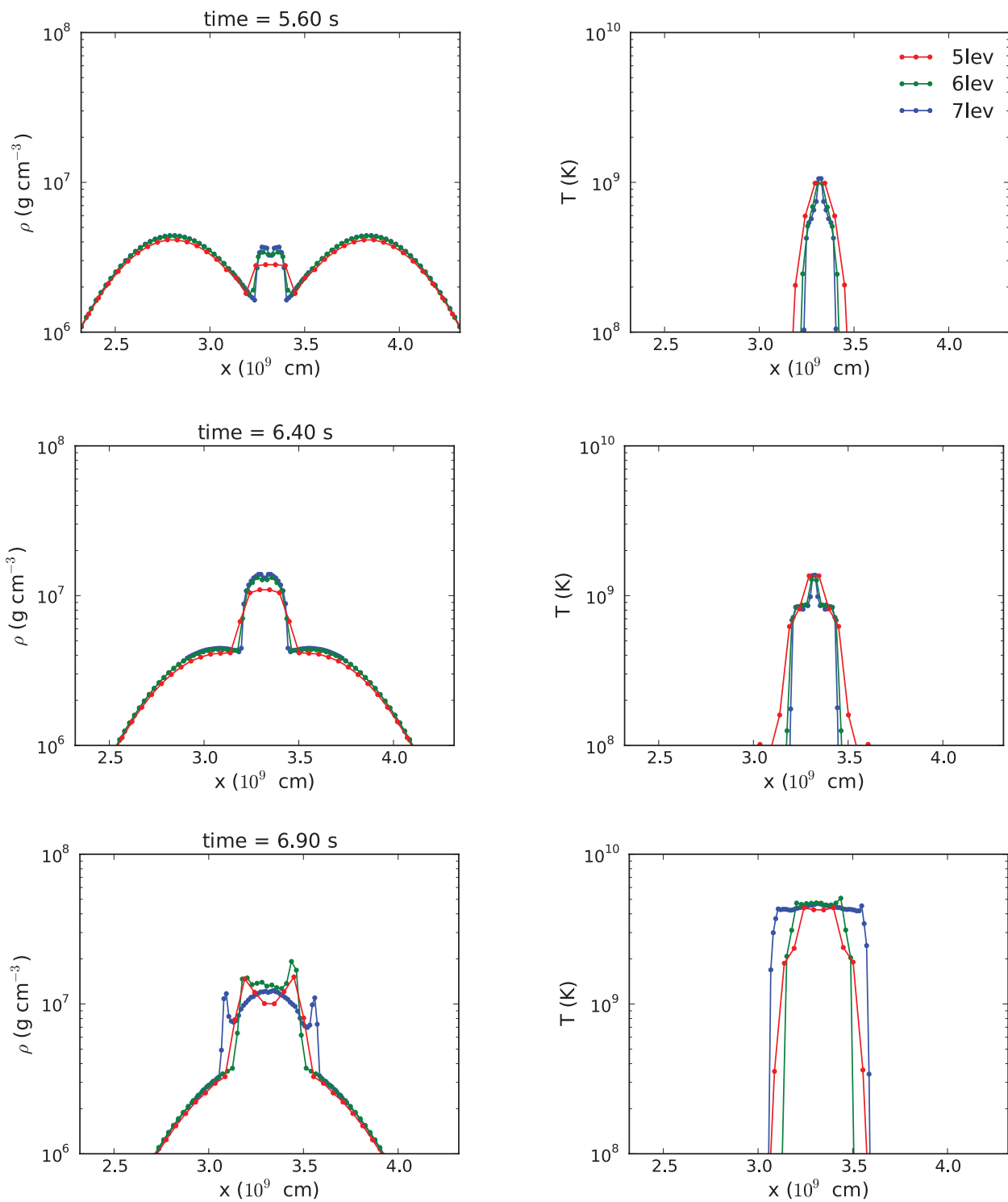


Fig. 10.— Density and temperature profiles along the x-axis for the  $2 \times 0.64$  collision at 5.6 s, 6.4 s, and 6.9 s for different levels of refinement.

with high density ( $> 10^7 \text{ g cm}^{-3}$ ) at the same ignition temperature. We also expect only a small difference in  $^{56}\text{Ni}$  production between the 6- and 7-level models because the peak density is only slightly larger for the 7-level model and the width of the density profile is approximately the same. This explains the pattern in the the abundance yields with spatial resolution in Fig. 8.

At 6.9 s (lower panel in Fig. 10) when the detonation is underway, the Mach number is larger in the 7-level model than the 5- and 6-level models because the pre-detonation density is larger. This causes the 7-level temperature profile to be wider than the 6-level or the 5-level. That is, the burning front travels farther for the same amount of time.

Unlike the  $2 \times 0.64$  collision, the  $2 \times 0.81$  collision produces less  $^{56}\text{Ni}$  as level of refinement increases (see Fig. 8). The upper panel of Fig. 11 shows the three models with different spatial resolutions for the  $2 \times 0.81$  collision at 4.0 s. The temperatures for all three resolutions are hot ( $> 3 \times 10^9 \text{ K}$ ), indicating the energy generated by burning is large. The shocked region is widest for the 7-level model and narrowest for the 5-level model with the 6-level model in-between. The 7-level model has the lowest, and nearly constant, density ( $\approx 8 \times 10^6 \text{ g cm}^{-3}$ ) in the stalled shock region, and has the largest magnitude spikes in the density (just below  $2 \times 10^7 \text{ g cm}^{-3}$ ) at the edges of the stalled shock. The spikes occur because the density of material is highest just behind the shock front. The 6-level model has a slightly larger ( $\approx 8 \times 10^6 \text{ g cm}^{-3}$ ), nearly constant, density in the middle, and slightly smaller spikes in the density (just below  $2 \times 10^7 \text{ g cm}^{-3}$ ) at its edges. The 5-level model has its density spikes (just above  $10^7 \text{ g cm}^{-3}$ ) close enough together that a nearly constant density in the middle is barely reached.

The second panel of Fig. 11 shows at 4.4 s the width of the shocked, burning region is larger for all three resolutions, because the energy generated by burning in the hot shocked region is sufficient to overcome the standing shock formed from material moving inwards.



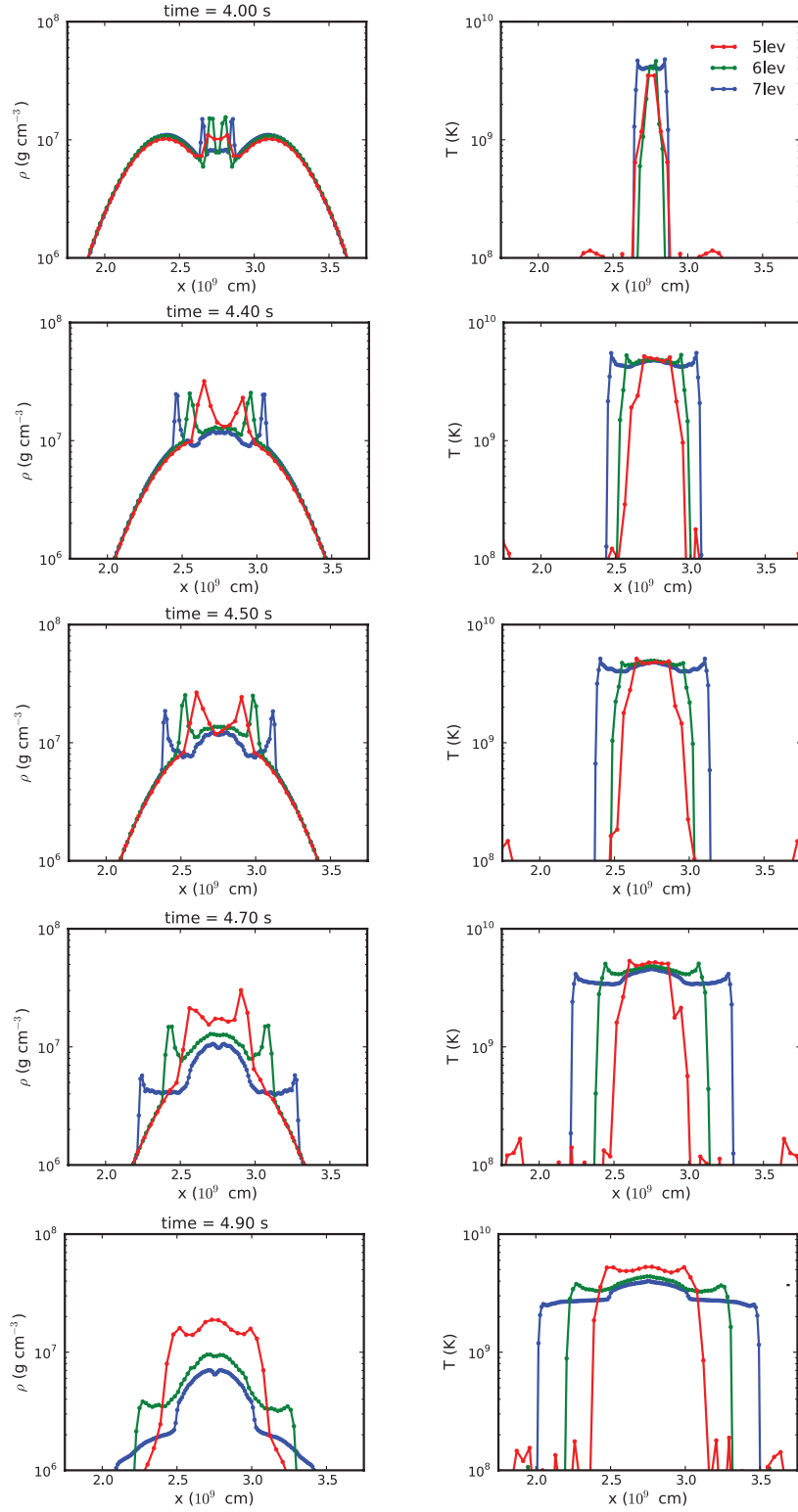


Fig. 11.— Density and temperature profiles along the x-axis for the  $2 \times 0.81$  collision at 4.0 s, 4.4 s, 4.5 s, 4.7 s, and 4.9 s for different levels of refinement.

That is, the shocked burning region is growing. The temperature is nearly the same and constant ( $\approx 5 \times 10^9$  K) across all three resolutions, but with small spikes at the edges of each shocked region. The nearly constant density in the central region of the 7-level model is still smaller and wider than the the 6-level model. The 5-level still has its two spikes near the center, thus a nearly constant central density region is not reached.

The third panel of Fig. 11 shows at 4.5 s the the 7 level model begins to detonate, but the 6-level and 5-level models have not yet detonated. The same patterns in density and temperature described for previous time points still hold. By 4.7 s, the fourth panel Fig. 11 shows the 6-level model begin to detonate, but the 5 level model has not yet detonated. The width of the burning region for the 6-level model is about the same width as the 7-level model when the 7-level model detonated 0.2 s earlier.

At 4.9 s (bottom panel Fig. 11), the 5-level model is the last to detonate. The 5-level model has finally reached a state of nearly constant density in the central region with spikes at the edges. This nearly constant density of  $2 \times 10^7$  g cm<sup>-3</sup> is larger than the nearly constant density reached by either the 6-level or the 7-level models (both about  $10^7$  g cm<sup>-3</sup>), but it has reached about the same width. Since the 7-level model detonates at the lowest density (but the same mass since all reach about the same width before detonating) and soonest in time, the 7-level model should produce the least amount of <sup>56</sup>Ni. The 5-level model detonates at a higher density (and same mass) and latest in time, thus should produce the most <sup>56</sup>Ni. This explains the pattern in the the abundance yields with spatial resolution in Fig. 8.

### 3.3. Similarities and Differences Between the Explosion Models

Whether the explosion is initiated along the edge of the stalled shock region (as in the  $2\times 0.81$  collisions) or in the central regions of the stalled shock (as in the  $2\times 0.64$  collisions) is controlled by the initial masses of the white dwarfs, as the masses set the infall speed (escape velocity). The infall speed determines the strength of the initial shock, and thus the initial post-shock temperature. In turn, the initial post-shock temperature determines the amount of initial burning behind the shock, and hence the temperature profile of the shocked region. Comparing the temperatures profiles in the shocked region between the  $2\times 0.64$  and  $2\times 0.81$  collisions, we see that the  $2\times 0.64$  temperature barely reaches  $10^9$  K, while for the  $2\times 0.81$  temperature is a hot  $\approx 5 \times 10^9$  K over an extended region. The difference in the temperature between the two model collisions is a direct consequence of the kinetic energy of the collision (larger kinetic energy corresponding to larger temperature).

The initial shock in the  $2\times 0.64$  collision models barely raises the temperature above the  $^{12}\text{C}+^{12}\text{C}$  threshold. As carbon burning proceeds, the central shocked burning region increases in temperature. The top panel of Fig. 12) shows the system cannot explode yet because the temperature is not hot enough to overcome the ram pressure from the infalling material, which continues to increase due to density profile of the white dwarf. When the peak of the white dwarf density profiles enters the shocked region does the central peak undergo thermonuclear runaway, which creates enough pressure to overcome the now decreasing ram pressure (see bottom panel of Fig. 12).

In contrast to the  $2\times 0.64$  collision model, the  $2\times 0.81$  collision model is energetic enough that the initial shock raises the temperature well above the  $^{12}\text{C}+^{12}\text{C}$  threshold. The entire stalled shocked region burns rapidly to a state of nuclear statistical equilibrium and achieves a nearly isothermal state. Central ignition cannot occur because the  $^{12}\text{C}+^{16}\text{O}$  material has already lost nearly all of its energy in the burn to nuclear statistical equilibrium. The

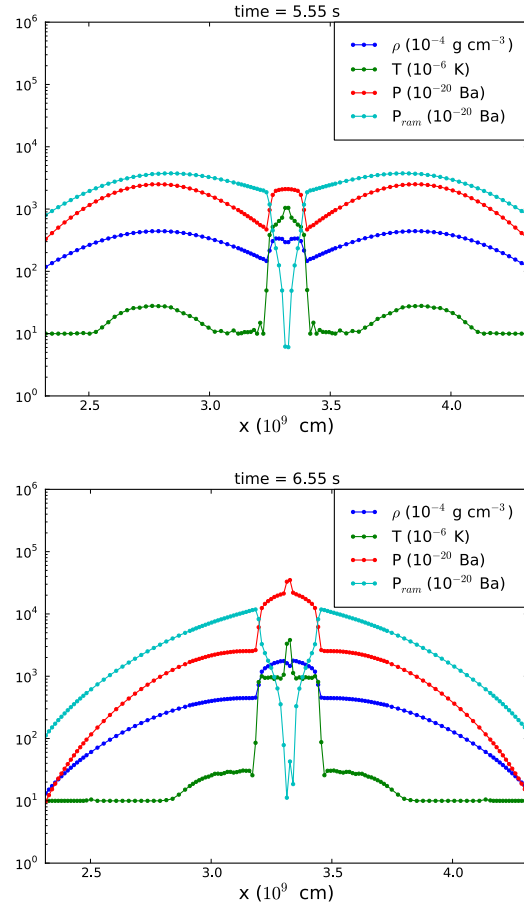


Fig. 12.— Profiles of the density, temperature, pressure, and ram pressure along the x-axis for the  $2 \times 0.64$  collision at 5.55 s and 6.55 s.

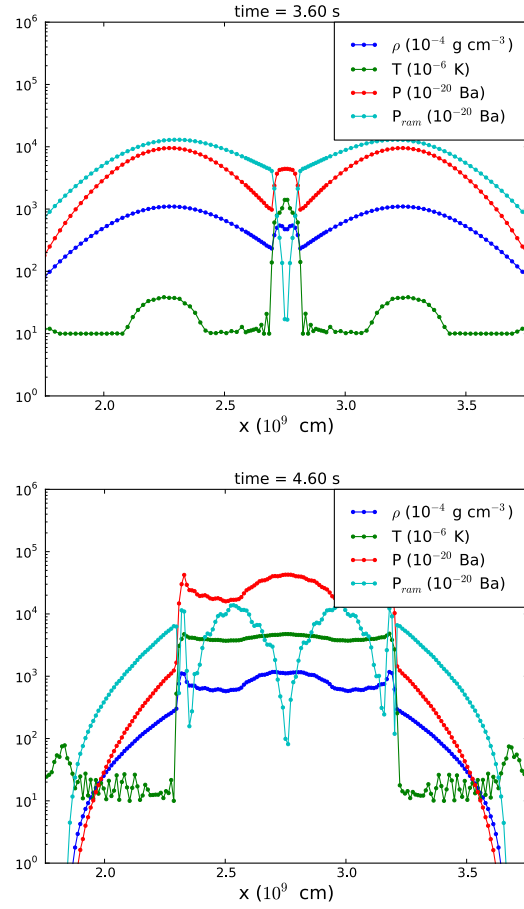


Fig. 13.— Density, temperature, pressure, and ram pressure profiles along the x-axis for the  $2 \times 0.81$  collision at 3.60 s and 4.60 s.

top panel of Fig. 12 shows, similar to the  $2\times 0.64$  collision models, the  $2\times 0.81$  collision model cannot yet explode since the ram pressure from the infalling material is greater than the pressure of the hot burned material pushing outwards. When the pressure inside the hot burned region is larger than the ram pressure does the system explode, giving the appearance of an edge-lit ignition (see bottom panel of Fig. 12).

#### 4. Discussion

We have performed the first systematic study of zero impact parameter collisions between two white dwarfs with an Eulerian grid code (FLASH). Our simulations spanned a range of effective spatial resolutions for collisions between two  $0.64 M_{\odot}$  white dwarfs and two  $0.81 M_{\odot}$  white dwarfs. However, even the highest resolution studies did not achieve strict numerical convergence.

The lack of convergence in the simplest configuration (zero impact parameter, equal masses) suggest that quantitative predictions of the ejected elemental abundances that are generated by binary white dwarf collision and merger simulations should be viewed with caution. However, the convergence trends do allow some patterns to be discerned.

We found the  $2\times 0.64$  collision model head-on collision model produces  $0.32 M_{\odot}$  of  $^{56}\text{Ni}$ ,  $0.38 M_{\odot}$  of  $^{28}\text{Si}$ , and  $0.2 M_{\odot}$  of unburned  $^{12}\text{C}+^{16}\text{O}$ . Rosswog et al. (2009) included one FLASH based model of a zero impact parameter collision of two  $0.60 M_{\odot}$  white dwarfs in their study. They reported a  $^{56}\text{Ni}$  mass of  $0.16 M_{\odot}$ , about one-half of what we find. While Rosswog et al. (2009) used slightly less massive white dwarfs than our study, both sets of FLASH simulations used the same equation of state. The FLASH model of Rosswog et al. (2009) achieved about a factor of 2.6 smaller spatial resolution than our study ( $R = 4.9 \times 10^6$  cm versus  $R = 1.3 \times 10^7$  cm), due to their evolving one white dwarf and deploying a

mirrored gravitational potential. This difference in the maximum spatial resolution could account for the different  $^{56}\text{Ni}$  masses between the two calculations, although the convergence trend shown in the upper panel Fig. 8 suggests spatial resolution might not be the only reason for the difference. Another potential reason for the difference in the  $^{56}\text{Ni}$  masses is the choice of the timestep, and thus the coupling between the operator split processes of hydrodynamics and the nuclear burning. In all our simulations, we limited the timestep to  $\approx 0.01$  of the Courant limited hydrodynamic timestep during the nuclear burning phases (see Fig. 9). We found changing the allowed timestep can change the  $^{56}\text{Ni}$  mass produced by 30% - 40%.

We find our FLASH-based, zero impact parameter, collision models systematically produce less  $^{56}\text{Ni}$  and more silicon-group elements than collisions models calculated with SNSPH by Raskin et al. (2010). This difference between particle and grid based codes was first found by Rosswog et al. (2009), who suggested that differences in nuclear reaction networks or advection effects could be responsible for the different yields. While our FLASH models used the same equation of state and nuclear reaction network as Raskin et al. (2010), and we checked the same output values were returned for the same input values, a detailed investigation of the differences between our FLASH model results and the Raskin et al. (2010) results with SNSPH are beyond the scope of this paper.

Red and dim SNIa such as SN 1991bg (Leibundgut et al. 1993; Turatto et al. 1996; Hachinger et al. 2009) SN 1992K (Hamuy et al. 1994), SN 1999by (Garnavich et al. 2004), and SN 2005bl (Taubenberger et al. 2008) are characterized by  $M_V \approx -17$ . The light curves of underluminous SNIa decline even more rapidly than expected from a linear luminosity to decline-rate relation among normal SNIa (Phillips et al. 1999; Taubenberger et al. 2008; Blondin et al. 2012). Spectroscopically, 91bg-like SNIa show low line velocities around B-magnitude maximum (Filippenko et al. 1992) and clear spectral signatures of Ti-II,

indicating lower ionization (Mazzali et al. 1997). Taken together, these properties together are consistent with  $\sim 0.1 M_{\odot}$  of newly synthesized  $^{56}\text{Ni}$ . Our FLASH models suggest  $2 \times 0.64 M_{\odot}$  and  $2 \times 0.81 M_{\odot}$  head-on collision models produce  $^{56}\text{Ni}$  masses below that needed for normal SNIa, but are within a range consistent with observations of underluminous SNIa. In addition, either mass pairing produces  $\sim 0.2 M_{\odot}$  of unburned C+O, which may be a unique signature of mergers and collisions between white dwarfs.

Future studies should include a survey of non-zero impact parameter white dwarf collisions with FLASH, an exploration of unequal mass collisions, and an investigation why Lagrangian particles codes and Eulerian grid codes continue to find about a factor of two difference in the mass of  $^{56}\text{Ni}$  ejected. The zero impact parameter is insightful as an upper limit on  $^{56}\text{Ni}$  production, but a non-zero impact parameter study will likely give a range of  $^{56}\text{Ni}$  yields for different collision configurations. An exploration of unequal mass collisions could provide a broader physical parameter space and allow an improved quantitative description of how SNIa luminosity scales with mass pairings.

## 5. Acknowledgments

This work was supported by the National Science Foundation under grant AST 08-06720 and through the Joint Institute for Nuclear Astrophysics (JINA) under grant PHY 02-16783. All simulations were conducted with Arizona State University Advanced Computing Center and Extreme Science and Engineering Discovery Environment (XSEDE) compute resources. FLASH was in part developed by the DOE-supported ASC/Alliances Center for Astrophysical Thermonuclear Flashes at the University of Chicago. Wendy Hawley thanks Brandon Mechtley for his invaluable computing assistance.



## REFERENCES

- Benz, W., Cameron, A. G. W., Press, W. H., & Bowers, R. L. 1990, *ApJ*, 348, 647
- Benz, W., Thielemann, F., & Hills, J. G. 1989, *ApJ*, 342, 986
- Bianco, F. B., Howell, D. A., Sullivan, M., et al. 2011, *ApJ*, 741, 20
- Blondin, S., Matheson, T., Kirshner, R. P., et al. 2012, *AJ*, 143, 126
- Branch, D., Fisher, A., & Nugent, P. 1993, *AJ*, 106, 2383
- Calder, A. C., Fryxell, B., Plewa, T., et al. 2002, *ApJS*, 143, 201
- Dan, M., Rosswog, S., Guillochon, J., & Ramirez-Ruiz, E. 2011, *ApJ*, 737, 89
- Filippenko, A. V., Richmond, M. W., Branch, D., et al. 1992, *AJ*, 104, 1543
- Fryxell, B., Olson, K., Ricker, P., et al. 2000, *ApJS*, 131, 273
- Garnavich, P. M., Bonanos, A. Z., Krisciunas, K., et al. 2004, *ApJ*, 613, 1120
- Gilfanov, M., & Bogdán, Á. 2010, *Nature*, 463, 924
- Guerrero, J., García-Berro, E., & Isern, J. 2004, *A&A*, 413, 257
- Hachinger, S., Mazzali, P. A., Taubenberger, S., Pakmor, R., & Hillebrandt, W. 2009, *MNRAS*, 399, 1238
- Hamuy, M., Phillips, M. M., Maza, J., et al. 1994, *AJ*, 108, 2226
- Hicken, M., Garnavich, P. M., Prieto, J. L., et al. 2007, *ApJ*, 669, L17
- Howell, D. A., Sullivan, M., Nugent, P. E., et al. 2006, *Nature*, 443, 308
- Leibundgut, B., Kirshner, R. P., Phillips, M. M., et al. 1993, *AJ*, 105, 301

- Lorén-Aguilar, P., Isern, J., & García-Berro, E. 2009, *A&A*, 500, 1193
- . 2010, *MNRAS*, 406, 2749
- Maoz, D. 2008, *MNRAS*, 384, 267
- Mazzali, P. A., Chugai, N., Turatto, M., et al. 1997, *MNRAS*, 284, 151
- Pakmor, R., Kromer, M., Röpke, F. K., et al. 2010, *Nature*, 463, 61
- Pakmor, R., Kromer, M., Taubenberger, S., et al. 2012, *ApJ*, 747, L10
- Perlmutter, S., Aldering, G., Goldhaber, G., et al. 1999, *ApJ*, 517, 565
- Phillips, M. M. 1993, *ApJ*, 413, L105
- Phillips, M. M., Lira, P., Suntzeff, N. B., et al. 1999, *AJ*, 118, 1766
- Rasio, F. A., & Shapiro, S. L. 1995, *ApJ*, 438, 887
- Raskin, C., Scannapieco, E., Fryer, C., et al. 2012, *ApJ*, 746, 62
- Raskin, C., Scannapieco, E., Rockefeller, G., et al. 2010, *ApJ*, 724, 111
- Raskin, C., Timmes, F. X., Scannapieco, E., Diehl, S., & Fryer, C. 2009, *MNRAS*, 399, L156
- Ricker, P. M. 2008, *ApJS*, 176, 293
- Riess, A. G., Filippenko, A. V., Challis, P., et al. 1998, *AJ*, 116, 1009
- Riess, A. G., Macri, L., Casertano, S., et al. 2011, *ApJ*, 730, 119
- Rosswog, S., Ramirez-Ruiz, E., & Hix, W. R. 2009, *ApJ*, 695, 404
- Shen, K. J., Bildsten, L., Kasen, D., & Quataert, E. 2012, *ApJ*, 748, 35

- Silverman, J. M., Foley, R. J., Filippenko, A. V., et al. 2012, ArXiv e-prints
- Sullivan, M., Guy, J., Conley, A., et al. 2011, ApJ, 737, 102
- Suzuki, N., Rubin, D., Lidman, C., et al. 2012, ApJ, 746, 85
- Taubenberger, S., Hachinger, S., Pignata, G., et al. 2008, MNRAS, 385, 75
- Thielemann, F.-K., Nomoto, K., & Yokoi, K. 1986, A&A, 158, 17
- Timmes, F. X. 1999, ApJS, 124, 241
- Timmes, F. X., & Swesty, F. D. 2000, ApJS, 126, 501
- Turatto, M., Benetti, S., Cappellaro, E., et al. 1996, MNRAS, 283, 1
- van Kerkwijk, M. H., Chang, P., & Justham, S. 2010, ApJ, 722, L157
- Whelan, J., & Iben, I. J. 1973, ApJ, 186, 1007
- Yoon, S.-C., Podsiadlowski, P., & Rosswog, S. 2007, MNRAS, 380, 933